Geodynamic, geodetic, and seismic constraints favour deflated and dense-cored LLVPs

Fred D. Richards [a],*, Mark J. Hoggard [b], Sia Ghelichkhan [b], Paula Koelemeijer [c,d], Harriet C.P. Lau [e,f]

[a] *Department of Earth Science & Engineering, Imperial College London, Royal School of Mines, Prince Consort Road, London, SW7 2AZ, UK*
[b] *Research School of Earth Sciences, Australian National University, 142 Mills Road, Acton, ACT 0200, Australia*
[c] *Department of Earth Sciences, Royal Holloway University of London, Egham Hill, Egham, TW20 0EX, UK*
[d] *Department of Earth Sciences, University of Oxford, South Parks Road, OX1 3AN, UK*
[e] *Department of Earth & Planetary Science, University of California, Berkeley, 307 McCone Hall, Berkeley, CA, 94720, USA*
[f] *Department of Earth, Environmental, and Planetary Sciences, Brown University, 324 Brook St., Providence, RI, 02912, USA*

ARTICLE INFO

ABSTRACT

Two continent-sized features in the deep mantle, the *large low-velocity provinces* (LLVPs), influence Earth's supercontinent cycles, mantle plume generation, and geochemical budget. Seismological advances have steadily improved LLVP imaging, but several fundamental questions remain unanswered, including: What is the true vertical extent of the buoyancy anomalies within these regions? And, are they purely thermal features, or are they also compositionally distinct? Here, we address these questions using a comprehensive range of geophysical observations. The relationship between measured geoid anomalies and long-wavelength dynamic surface topography places an important upper limit on the vertical extent of large-scale, LLVP-related density anomalies at ~900 km above the core-mantle boundary (CMB). Instantaneous mantle flow modelling suggests that anomalously dense material must exist at their base to simultaneously reproduce geoid, dynamic topography, and CMB ellipticity observations. We demonstrate that models incorporating this dense basal layer are consistent with independent measurements of semi-diurnal Earth tides and Stoneley mode splitting functions. Our thermodynamic calculations indicate that the presence of early-formed, chondrite-enriched basalt in the deepest 100–200 km of the LLVPs is most compatible with these geodynamic, geodetic, and seismological constraints. By reconciling these disparate datasets for the first time, our results demonstrate that, although LLVPs are dominantly thermal structures, their basal sections likely represent a primitive chemical reservoir that is periodically tapped by upwelling mantle plumes.

1. Introduction

Seismic tomographic models consistently image two large regions of slow seismic velocity in the deep mantle that are widely interpreted to be hotter than ambient material and are spatially correlated with positive, long-wavelength geoid height anomalies (Figs. 1 and 2a; Garnero et al., 2016). Early mantle flow studies treated these features as buoyant upwellings and found that an increase of mantle viscosity with depth is required to obtain satisfactory model fits to observed non-hydrostatic geoid height anomalies (Hager et al., 1985). Nevertheless, these instantaneous flow calculations are non-unique and suffer from trade-offs be-

tween the magnitude and distribution of excess buoyancy. While there is emerging consensus on the lateral extent of LLVPs (e.g., Cottaar and Lekic, 2016), numerous controversies remain concerning their structure and composition.

First, it is uncertain how high thermochemical heterogeneity associated with LLVPs extends above the CMB. Body wave coverage in the mid-to-lower mantle (~1000–2500 km depth) is limited, with most ray paths traversing this region near-vertically, making global tomographic models susceptible to smearing artefacts in this depth range (Ritsema et al., 2007; Koelemeijer et al., 2018). Recent studies have even suggested that laterally extensive low-velocity structures imaged at depths ≤2000 km may actually represent tomographic aliasing of clusters of distinct plumes (Davaille and Romanowicz, 2020).

Second, considerable debate remains over whether LLVPs are purely thermal or also compositionally distinct features. Isotopic
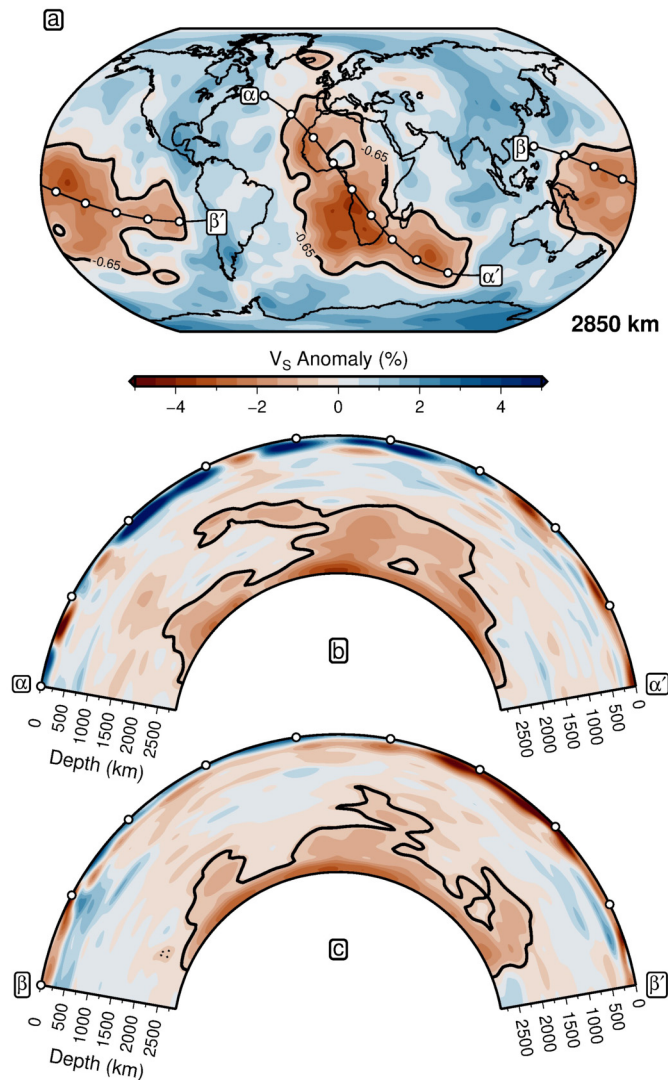
Fig. 1. Spatial extent of seismically imaged LLVPs. (a) Shear-wave velocity (V_S) anomalies at 2850 km depth in the TX2011 seismic tomographic model (Grand, 2002), which is used throughout this study. Thick black contour $= -0.65\%$ V_S anomaly threshold used to delineate LLVP boundaries (Torsvik et al., 2006; Lau et al., 2017); α–α' and β–β' = cross-section locations with white circles spaced at 1000 km intervals. (b) Cross-section α–α' beneath Africa through blended tomographic model (SLNAAFSA above 300 km, TX2011 below 400 km, linearly interpolated between 300–400 km; Grand, 2002; Hoggard et al., 2020). (c) Cross-section β–β' beneath Pacific Ocean. For interpretation of the colours in the figure(s), the reader is referred to the web version of this article.

variations in intraplate volcanic rocks (Arevalo et al., 2013), joint seismic-geodynamic inversions (Lu et al., 2020), body tides (Lau et al., 2017), and their apparent stability with respect to the reconstructed locations of Phanerozoic kimberlites and large igneous provinces (Burke et al., 2008), all suggest that LLVPs are enriched in chemically distinct and anomalously dense material. Numerical models suggest that this material must have a $\sim$2–4% intrinsic chemical density excess to generate and preserve such compositional heterogeneity over billion-year timescales (Tackley, 2012; Jones et al., 2020). Seismic evidence in favour of chemically distinct LLVPs has, however, proven less conclusive. For example, the decorrelation between shear-wave velocity (V_S) and bulk sound velocity (V_ϕ) below 2000 km depth has been inferred to support both thermal and thermochemical interpretations (Koelemeijer et al., 2018). Similarly, strong lateral V_S gradients at LLVP boundaries may point to chemical heterogeneity (Ni et al., 2002), but several studies suggest that similar features may occur with purely thermal variations

(e.g., Schuberth et al., 2009; Davies et al., 2012). While normal mode studies generally prefer anomalously dense LLVPs (Moulik and Ekström, 2016), recent Stoneley mode observations (i.e., normal modes trapped along the CMB) indicate that LLVPs are, on average, positively buoyant, although a $\sim$ 100 km-thick, anomalously dense basal layer cannot be ruled out (Koelemeijer et al., 2017). This result apparently contradicts inferences from body tide observations, which yield a mean excess density of $\sim$ 1% within the bottom $\sim$ 350 km of the LLVPs (Lau et al., 2017).

While LLVP buoyancy structure remains uncertain, their morphology and the potential presence of chemically distinct basal material is expected to significantly influence spatiotemporal patterns of mantle circulation (Gurnis et al., 2000; Lu et al., 2020). Since the earliest models of global mantle flow (Hager et al., 1985), there have been several important advances in geodynamic observables, notably improved present-day constraints on excess ellipticity of the CMB (Dehant et al., 2017) and the planform of surface dynamic topography (Hoggard et al., 2016). Moreover, recent geodetic and seismological measurements of Earth's long-period motions—in particular, body tides and Stoneley modes—now provide additional bounds on deep mantle density structure (Koelemeijer et al., 2017; Lau et al., 2017). These developments allow us to investigate the trade-off between the magnitude and distribution of LLVP buoyancy, and to re-examine associated controversies using new simulations of whole-mantle flow, tidal deformation and Stoneley mode oscillations.

In this study, we undertake three distinct but related analyses. First, we perform geodynamic inversions using a suite of existing tomographic models to determine the vertical extent of LLVPs and whether thermal or thermochemical density structures are more compatible with observations of the geoid, CMB ellipticity, and dynamic topography. Secondly, the best-fitting density configurations are tested against independent Stoneley mode splitting and body tide measurements, and we demonstrate for the first time that the existing discrepancies between these datasets can be resolved. Thirdly, we explore geochemical implications of these inversion-derived buoyancy structures using thermodynamic calculations of density and elastic properties of possible compositional endmembers for LLVP thermochemical heterogeneity. By analysing fits of the resulting model predictions with a wide range of observations, we constrain the nature and distribution of long-wavelength chemical heterogeneity within the deep Earth.

2. Geodynamic inversions

Recent re-evaluation of dynamic surface topography using global inventories of residual depth measurements confirms that the long-wavelength component of this field is spatially correlated with geoid height anomalies (Fig. 2a and b; Hoggard et al., 2016, 2017). While there is some disagreement on the appropriate methodology for spectrally analysing these data, studies have converged on water-loaded amplitudes of ±700 m at spherical harmonic degrees $l = 1$–3 (Hoggard et al., 2016; Watkins and Conrad, 2018; Steinberger et al., 2019; Valentine and Davies, 2020). Meanwhile, for its CMB counterpart, geodetic observations of Earth's free core nutation place a narrow bound of $\sim 400 \pm 100$ m on the amplitude of the degree-two ($l = 2$), order-zero ($m = 0$) component of non-hydrostatic CMB topography (i.e., excess ellipticity; Fig. 2c; Dehant et al., 2017). Unfortunately, efforts to map global CMB topography at shorter wavelengths using seismic data are presently hampered by trade-offs between velocity and density structure in the D'' region (Koelemeijer, 2021).

In light of these improved and revised constraints, we ask: Can a model of V_S-derived mantle density be constructed that simultaneously satisfies the geoid, dynamic topography, and excess CMB ellipticity? To investigate this issue, we construct a suite of $\sim 10^6$

density models, simulate the resulting instantaneous mantle flow, and compute misfits to the observational data sets to invert for optimal thermal and thermochemical models of mantle density.

2.1. Data and methods

2.1.1. Constructing thermal and thermochemical mantle density models

Flow within the mantle is responsible for generating geoid anomalies, CMB and surface dynamic topography, and is driven by buoyancy anomalies within its interior. To simulate this flow, we generate initial input density models by dividing the mantle into six layers: 0–400 km (UUM = upper upper mantle), 400–670 km (LUM = lower upper mantle), 670–1000 km (UMM = upper mid-mantle), 1000–2000 km (LMM = lower mid-mantle), 2000–2700 km (ULM = upper lower mantle), and 2700–2891 km (LLM = lower lower mantle). The depth of each boundary was chosen to allow for abrupt changes in bulk physical properties across proposed viscosity jumps and major phase transitions (e.g., olivine−wadsleyite, wadsleyite–ringwoodite, iron spin transition, and perovskite–post-perovskite).

Within the UMM layer, seismic velocities are converted into density following the methodology of Richards et al. (2020), wherein a range of observational constraints on the covariation of V_S, temperature, attenuation and viscosity in Earth's upper mantle are used to invert for best-fitting parameters in an experimentally derived model of anelasticity at seismic frequencies (Yamauchi and Takei, 2016). Key advantages of this approach are that it allows thermomechanically self-consistent mapping between seismic velocities and temperature, density, and viscosity variations, while also correcting for discrepancies between tomographic models that result from parameterisation choices rather than true Earth structure. The tomographic V_S model we use to obtain upper mantle densities is SLNAAFSA, a version of the SL2013sv (Schaeffer and Lebedev, 2013) upper mantle model into which a number of high-resolution regional updates have been incorporated (see Hoggard et al., 2020 for details). This input V_S structure is chosen since the baseline model, SL2013sv, has already been shown to produce topographic predictions that are in good agreement with residual depth measurements, even at relatively short wavelengths (~ 1000 km; Richards et al., 2020). Optimal anelasticity parameters determined for SLNAAFSA are: $\mu_0 = 75.9$ GPa; $\frac{\partial \mu}{\partial T} = -17.9$ MPa °C^{-1}; $\frac{\partial \mu}{\partial P} = 2.54$; $\eta_r = 10^{23.0}$ Pa s; $E_a = 489$ kJ mol^{-1}; $V_a = 0.63$ cm^3 mol^{-1}; and $\frac{\partial T_s}{\partial z} = 0.931$ °C km^{-1}.

We assume that continental lithosphere, delineated by the $T = 1200$ °C isothermal surface, has neutral buoyancy and set density in these regions equal to the average density of all external material at the relevant depth in order to eliminate any direct dynamic topographic contribution. This assumption is based on heat flow measurements, xenolith geochemistry, seismic velocity, gravity, and topography observations that suggest compositional and thermal density contributions approximately balance each other within the continental lithosphere (Jordan, 1978). We also remove systematic age-dependent increases in density associated with lithospheric cooling so that density anomalies are defined with respect to the same reference structure as is used to define the Hoggard et al. (2017) residual depth measurements. We note that, no matter how we chose to define residual depth anomalies (e.g., with respect to a half-space cooling model, a plate cooling model, or no model at all), our results are unaffected provided that upper mantle buoyancy anomalies are calculated with respect to a consistent reference density structure (Section S1.1; Fig. S7).

Deeper than 300 km, seismic velocity perturbations from whole-mantle tomographic models LLNL-G3D-JPS (Simmons et al., 2015), S40RTS (Ritsema et al., 2011), SAVANI (Auer et al., 2014), SEMUCB-WM1 (French and Romanowicz, 2015), and TX2011 (Grand, 2002) are initially converted into density variations around a

mean value by assuming a constant V_S-to-density scaling factor, $R_\rho = \partial \ln \rho / \partial \ln V_S$, within each layer. The corresponding mean absolute density at each depth is assumed to be equal to PREM (Dziewonski and Anderson, 1981). To ensure a smooth transition in density anomalies between the uppermost mantle and underlying layers, we take the weighted average of these two density models between 300 km and 400 km, beyond which the sensitivity of the surface-wave-dominated upper mantle model tends to zero. Weighting coefficients of the respective tomographic models, w_{UM} and w_{WM}, vary linearly between 1 and 0 over this depth range and are calculated according to $w_{UM} = 1 - w_{WM}$. R_ρ is fixed at 0.15 for the whole-mantle model between 300–400 km, based on the mean value within this layer inferred from SLNAAFSA.

The lower mantle layers, ULM and LLM, are laterally subdivided into regions outside (OULM and OLLM) and within the LLVPs (LULM and LLLM), with the boundary between each domain delineated using the -0.65% V_S anomaly contour of the respective whole-mantle tomographic model under investigation (Torsvik et al., 2006; Lau et al., 2017). Note that there is considerable topography on the LLVP boundaries since, rather than projecting the -0.65% V_S anomaly contour vertically upwards from the CMB, we apply this dividing line to each depth slice (see Fig. 1b and c). Within each layer, we vary the V_S-to-density scaling factor as $R_\rho = [0.1, 0.2, 0.3, 0.4]$. These values span expectations from mineral physics constraints on pyrolitic and mixed pyrolitic-basaltic compositions, which are both hypothetical compositions for an isochemical mantle (Deschamps et al., 2012; Lu et al., 2020). To allow for limited seismic resolution and the potential presence of imaging artefacts due to vertical tomographic smearing in the lower mid-mantle (1000–2000 km), we also test a value of $R_\rho = 0$ for the LMM layer. It is generally expected that the impact of anelasticity and presence of phase transitions may introduce non-linearity into the V_S-to-density relationship. Nevertheless, the computational expense of fully exploring the parameter space in the first stage of our analysis necessitates the use of linear scaling factors (R_ρ) to describe these behaviours within the deeper mantle. We believe that this simplification is justified since anelastic effects are anticipated to be weak throughout most of the lower mantle and layer boundaries have been positioned to coincide with major phase transitions, thereby permitting a first-order approximation of these effects.

Across LLVP boundaries, we allow a constant compositional density anomaly, $\delta \rho_c(i)$, in addition to thermal effects such that $\delta \rho(z) = R_\rho(i) \delta V_S(z) + \delta \rho_c(i)$ within the LLVPs, where z is depth and i is the layer index (i.e., ULM or LLM). Thus, $\delta \rho_c(i)$ corresponds to the intrinsic compositional density difference between LLVP material and surrounding mantle material under ambient conditions. Note that, in contrast to studies that employ negative R_ρ values (e.g. Moulik and Ekström, 2016; Koelemeijer et al., 2017; Lau et al., 2017), this approach maximises intra-LLVP density around the edges of the low-velocity regions rather than within their central portions, and therefore assumes that, within each compositional domain, internal V_S variations are controlled by temperature in the usual manner (Fig. S8). This configuration is therefore consistent with the hypothesis that sharp compositional contrasts may be responsible for strong lateral gradients in V_S across the LLVP boundaries (Ni et al., 2002). In these initial thermal and thermochemical models, $\delta \rho_c$ varies as $[0., 0.2, .., 2.0]\%$ within the LULM and LLLM regions, yielding a total of $\sim 2 \times 10^5$ input density structures. In the Supplementary Information, we also test the effects of parameterising excess LLVP density using negative R_ρ values (instead of an intrinsic density contrast) and defining the ULM-to-LLM boundary at 2800 km rather than 2700 km (Section S1.2).

2.1.2. Simulating present-day mantle flow

We next use this suite of mantle density models to predict geoid undulations, surface and CMB dynamic topography using an instantaneous flow kernel methodology for spherical harmonic degrees, l, from 1–30. As Earth's viscosity structure is uncertain, we assess the sensitivity of our mantle flow results using three different radial viscosity profiles that have been constrained by geoid, heat flow and glacial isostatic adjustment observations: S10 (Steinberger et al., 2010); F10V1 (Forte et al., 2010); and F10V2 (Forte et al., 2010).

To calculate instantaneous mantle flow, we exploit the sensitivity kernel methodology implemented by Hager et al. (1985) and extended by Corrieu et al. (1995) to account for the effects of compressibility. We impose free-slip surface and CMB boundary conditions. For each assumed viscosity profile, the resulting sensitivity kernels, K^l, vary as a function of depth and the spherical harmonic degree under consideration. Dynamic topography δA^{lm} can be determined using

$$\delta A^{lm} = \frac{1}{\Delta \rho_0} \int_{R_C}^{R_\oplus} K_A^l(r) \delta \rho^{lm}(r) dr \tag{1}$$

where K_A^l is the dynamic topography kernel, r is radius, $\Delta \rho_0$ is the density difference between the uppermost mantle ($\rho_0 = 3380$ kg m^{-3}; Dziewonski and Anderson, 1981) and water ($\rho_w = 1030$ kg m^{-3}), l and m are spherical harmonic degree and order, $R_\oplus = 6371$ km and $R_C = 3480$ km are the radii of the Earth and CMB, respectively, and $\delta \rho^{lm}(r)$ represents the driving buoyancy anomalies within a spherical harmonic expansion. The geoid, δN^{lm}, is calculated using

$$\delta N^{lm} = \frac{4\pi \gamma R_\oplus}{(2l+1) g_{R_\oplus}} \int_{R_C}^{R_\oplus} K_N^l(r) \delta \rho^{lm}(r) dr \tag{2}$$

where K_N^l is the geoid kernel, $g_{R_\oplus}$ is surface gravity and γ is the gravitational constant. CMB topography, δC^{lm}, is determined according to

$$\delta C^{lm} = -\frac{1}{\Delta \rho_C} \int_{R_C}^{R_\oplus} K_C^l(r) \delta \rho^{lm}(r) dr \tag{3}$$

where K_C^l is the CMB topography kernel and $\Delta \rho_C$ is the density difference between the lowermost mantle ($\rho_C = 5570$ kg m^{-3}) and the uppermost outer core ($\rho_{OC} = 9900$ kg m^{-3}; Dziewonski and Anderson, 1981).

Applying this kernel formalism permits rapid calculation of key observables and enables extensive exploration of the mantle density parameter space. The method cannot, however, incorporate lateral viscosity variations (LVVs). While LVVs are undoubtedly present within the mantle, several previous studies have concluded that they generate minimal differences in the geodynamical observations explored herein compared with those resulting from variability in the mantle density inputs derived from different tomographic models (e.g., Moucha et al., 2007; Lu et al., 2020). We therefore anticipate that our conclusions will remain valid for reasonable amplitudes of LVV.

2.1.3. Assessing misfit to geodynamic observations

We assess model performance using a combined misfit function to assess compatibility with geoid, dynamic topography and excess CMB ellipticity constraints. Following previous studies (e.g. Steinberger and Holme, 2008; Simmons et al., 2009), we define the misfit to geoid and dynamic topography based on variance reduction (VR), a proxy for the proportion of observed signal explained by a given model prediction. Geoid misfit, χ_N, is defined to be equivalent to $1 - VR_N$, where VR_N represents geoid variance reduction, and is calculated globally using

$$\chi_N = \frac{\sum_{l=2}^{l_{max}} \sum_{m=-l}^{l} \left(N_c^{lm} - N_o^{lm} \right)^2}{\sum_{l=2}^{l_{max}} \sum_{m=-l}^{l} \left(N_o^{lm} \right)^2} \tag{4}$$

where N^{lm} terms represent spherical harmonic coefficients of observed (subscript o) and predicted (subscript c) geoid, and $l_{max} = 30$ is the maximum spherical harmonic degree. Dynamic topography misfit, χ_A, is defined analogously to χ_N (i.e., $\chi_A = 1 - VR_A$). However, since accurate residual depth measurements only exist at specific oceanic locations, rather than comparing spherical harmonic coefficients, we instead determine this value in the spatial domain according to

$$\chi_A = \frac{\sum_{n_A=1}^{N_A} \left[\left(A_c^i - A_o^i \right) - \overline{\left(A_c^i - A_o^i \right)} \right]^2}{\sum_{n_A=1}^{N_A} \left(A_o^i - \overline{A_o^i} \right)^2} \tag{5}$$

where overlines indicate sample means and A^i terms are predicted and observed dynamic topography at $N_A = 2278$ geographic locations (Hoggard et al., 2017), sampled in each case from the spherical harmonic representations of these fields ($1 \leq l \leq 30$) to ensure that the two signals are being compared at a consistent set of spatial wavelengths. We note that the impact of lithospheric flexure on the observed field is minimal since, throughout the oceanic realm, flexural wavelengths are expected to be shorter than the smallest wavelengths considered in this study ($l = 30$ corresponds to spatial wavelengths of ~1300 km; Watts and Moore, 2017). In addition, the underlying residual topography compilation carefully excises data from regions with strong flexural signals, such as trenches, seamounts, and fracture zones (Hoggard et al., 2017). For the excess CMB ellipticity, since it is defined using a single spherical harmonic coefficient, we use

$$\chi_C = \sqrt{\left(\frac{C_c^{20} - C_o^{20}}{\sigma_{C_o^{20}}} \right)^2} \tag{6}$$

rather than using a variance-reduction-based misfit definition, which is similar to previous studies (Steinberger and Holme, 2008; Simmons et al., 2009). C^{20} terms represent the $l = 2$, $m = 0$ coefficient of observed and modelled CMB topography, and $\sigma_{C_o^{20}} = 100$ m based on the range of reported values (Gwinn et al., 1986; Dehant et al., 2017). Finally, we sum each of these three components into a combined geodynamic misfit function,

$$\chi_G = \chi_N + \chi_A + \chi_C. \tag{7}$$

2.2. Results: best-fitting models from geodynamic inversions

2.2.1. Deep mantle thermochemical structure

Three key results emerge from this analysis. First, we find that acceptable fits to both the geoid and dynamic surface topography can be obtained for both thermal and thermochemical density models (Figs. 2, 3, and S1–S6; Table S1). Second, we obtain lower misfits, higher correlation coefficients, and greater variance reductions for models that include compositionally distinct material in the LLVPs relative to purely thermal models. This difference is par-
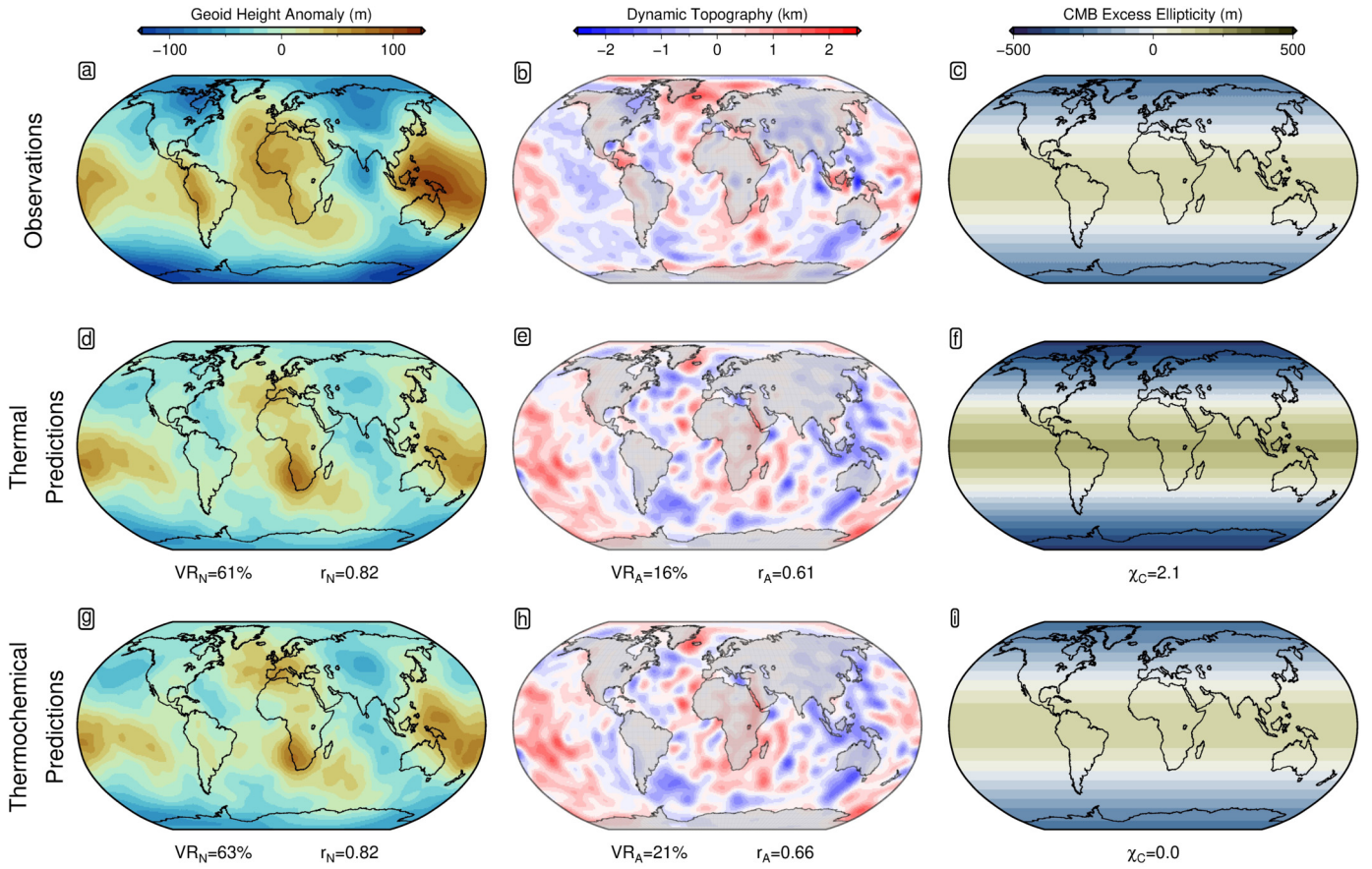
Fig. 2. Observations versus optimal instantaneous flow modelling predictions for the TX2011 tomographic model and S10 viscosity profile. (a) Observed non-hydrostatic geoid height anomalies (Chambat et al., 2010). (b) Observed dynamic surface topography (Hoggard et al., 2017). Grey shading = continental dynamic topography, approximated from long-wavelength free-air gravity anomalies using a constant admittance of $+50$ mGal km^{-1}. Note that this is a spherical harmonic representation ($1 \leq l \leq 30$) of the underlying data compilation, determined using the inverse approach of Hoggard et al. (2016). Continental regions are excluded from misfit analyses in this study due to the larger uncertainties on continental estimates of dynamic topography. (c) Observed excess CMB ellipticity (Dehant et al., 2017). (d) Predicted geoid for optimal mantle density model assuming LLVPs are purely thermal features. VR = variance reduction; r = Pearson's correlation coefficient. (e) Predicted dynamic topography for this model. (f) Predicted excess CMB ellipticity for this model. χ_C = misfit to observed CMB excess ellipticity (Equation 6). (g–i) Same for optimal density model that includes compositionally distinct LLVPs. Input elastic and density structure is obtained from the TX2011 model and the S10 viscosity profile is used to compute the mantle flow field.

ticularly clear for the excess CMB ellipticity (Fig. 2f versus i). Thermochemical models generally prefer strong excess density within the LLVP portion of the D″ layer ($\delta\rho_c \geq +0.8\%$ for 13 of 15 tomographic and viscosity model combinations), but find little to no excess density in the shallower 2000–2700 km depth range ($\delta\rho_c \leq +0.2\%$ for 13 of 15 models; Fig. 4d and e; Table S3). The thermochemical models also generally return R_ρ values throughout the middle (400–1000 km) and lower (2000–2900 km) mantle that are in better agreement with experimental expectations for a pyrolitic composition (Fig. 4a, b, d, and e; Deschamps et al., 2012; Lu et al., 2020). Third, all best-fitting models require $R_\rho \sim 0$ for the 1000–2000 km mid-mantle layer, irrespective of whether or not LLVP regions are modelled as compositionally distinct (Section S1.1 and 1.2; Fig. 4c; Tables S2 and S3).

We present optimal results for the S10 viscosity profile (Steinberger et al., 2010) and TX2011 tomographic model (Grand, 2002) only in Figs. 2 and 3b and d, since this tomographic model generates geodynamic predictions with the lowest overall misfit. However, results for other viscosity–tomography pairings are shown in the Supplementary Information (Figs. S1–S6) and demonstrate that the findings outlined above apply to all model configurations. Note that the geoid variance reduction we obtain for some of these models is lower than in previous work (e.g., Steinberger and Holme, 2008) because we do not directly optimise our radial viscosity structure to fit observed geoid undulations.

2.2.2. Vertical extent of LLVPs

Our geodynamic inversions exhibit a preference for $R_\rho \sim 0$ throughout the mid-mantle. This value is incompatible with plausible mantle compositions and indicates that V_S structure is not correlated with thermal buoyancy anomalies at these depths. Given that most seismic tomographic models exhibit substantial V_S structure at $l = 2$ over the 1000–2000 km depth range, we explore this intriguing result further using associated sensitivity kernels for instantaneous mantle flow.

The geoid-to-topography amplitude ratio (GTR) at $l = 2$ provides a crucial constraint on the vertical extent of long-wavelength buoyancy anomalies associated with LLVPs. In Fig. 5a and b, we show the $l = 2$ components of observed non-hydrostatic geoid height anomalies and water-loaded dynamic topography, which yield an estimated GTR of $\sim 0.21 \pm 0.07$. These deflections must be caused by $l = 2$ density anomalies, with the strongest corresponding shear-wave velocity (V_S) anomalies found within the LLVP regions, the mantle transition zone, and the asthenosphere (Fig. 5e). These V_S anomalies are anti-correlated with the observed geoid and dynamic topography, with the exception of the transition zone, where V_S anomalies correlate with the geoid but remain anti-correlated or become decorrelated with dynamic topography (Fig. 5f and g).

Individual $l = 2$ sensitivity kernels for the geoid, dynamic topography, and GTR (Fig. 5f–h) are sensitive to the choice of mantle viscosity profile (Fig. 5d), but their shape is broadly consistent
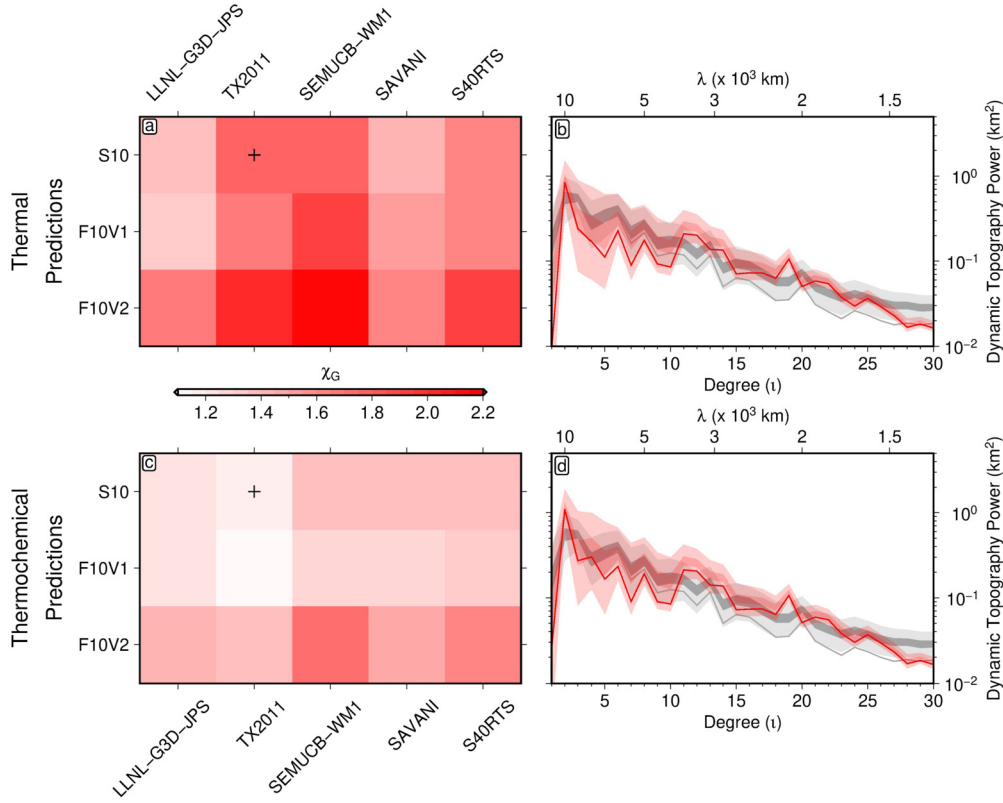
Fig. 3. Geodynamic misfit as a function of input density and viscosity model. (a) Total geodynamic misfit, χ_G (Equation 7), of best-fit thermal models for each combination of viscosity and seismic tomographic input. Black cross = model shown in (b) and Fig. 2d–f. (b) Observed and predicted dynamic topography power spectra of best-fit thermal model for TX2011 and S10 viscosity profile. Dark and light grey envelope = 99% and 50% confidence intervals for power spectrum of optimal spherical harmonic coefficients for oceanic residual depth measurements (intervals derived from 100,000 random samples of inverted spherical harmonic coefficient probability distributions; Valentine and Davies, 2020); solid grey line = power spectrum of mean spherical harmonic coefficients determined for oceanic residual depth measurements; dark and light red envelope = 99% and 50% confidence intervals for power spectrum of thermal model constructed by sampling predicted dynamic topography at locations of shiptrack and point-wise oceanic residual depth measurements and determining optimal spherical harmonic coefficients using Gaussian process-based methodology of Valentine and Davies (2020); solid red line = power spectrum of mean spherical harmonic coefficients determined for thermal model. (c) Total geodynamic misfit, χ_G, of best-fit thermochemical models for each combination of viscosity and seismic tomographic input. Black cross = model shown in (d) and Fig. 2g–i. (d) Observed and predicted dynamic topography power spectra of best-fit thermochemical model for TX2011 and S10 viscosity profile, as in (b).

for a range of published profiles (Fig. S9; Forte et al., 2010; Liu and Zhong, 2016). The $l = 2$ GTR kernel shows that, to satisfy the observed value of 0.21 ± 0.07, density anomalies must either anti-correlate with surface deflections in the deep mantle (intersection with red band in Fig. 5h) or positively correlate with the geoid—while remaining negatively correlated with dynamic topography—in the transition zone (intersection with blue band in Fig. 5h). Our analyses support the conclusions of previous studies (e.g., Hager et al., 1985) that it is deeper mantle structure that is the dominant contributor to the integrated GTR. These kernels also show that any $l = 2$, mid-mantle (∼1000–2000 km) thermal density anomalies can only lower the predicted GTR. A mantle density model with LLVPs extending shallower than ∼2000 km depth (i.e., more than ∼900 km above the CMB) that fits the observed geoid will therefore inevitably overpredict long-wavelength dynamic topography. Hence, the inversions return a preferred value of $R_\rho \approx 0$ in the mid-mantle. This finding provides strong evidence that long-wavelength, low-density anomalies associated with LLVPs do not vertically extend any further than 900 km above the CMB, which is consistent with recent arguments that seismically imaged $l = 2$, mid-mantle V_S structure is an artefact of limited tomographic resolution (Davaille and Romanowicz, 2020). Smaller scale density anomalies do exist in the 1000–2000 km depth interval (e.g., plumes and slabs; French and Romanowicz, 2015; Simmons et al., 2015); however, the corresponding instantaneous flow sensitivity kernels for shorter wavelengths approach zero over this depth range, such that these features have minimal impact on the geoid,

surface dynamic topography and CMB ellipticity. Indeed, geodynamic misfit changes by less than 10% when our optimised density fields are modified to suppress $l = 2$ structure while retaining shorter wavelength features between 1000–2000 km depth (by instead applying a high-pass filter and setting $R_\rho = 0.2$ within this layer; Section S1.3).

The finding that vertically compact LLVPs are required to simultaneously satisfy both geoid and dynamic topography observations likely explains why TX2011-based density models generate better overall fits to geodynamic observations. Unlike the other tomographic models tested in this work, lower mantle degree-two V_S anomalies are largely confined to depths greater than ∼ 2500 km in TX2011, the same depths where the $l = 2$ GTR kernel is most consistent with the observed GTR ratio (intersection with red band in Fig. 5h).

3. Tidal and Stoneley mode inversions

Body tides involve whole-Earth deformation in response to gravitational forces from the Moon and the Sun and, as such, are sensitive to deep mantle density structure (Lau et al., 2017). Stoneley modes are a class of free oscillation triggered by large earthquakes that are likewise sensitive to seismic velocity and density variations in the vicinity of the CMB (Koelemeijer et al., 2013). Despite similar, though not identical, sensitivity to deep Earth structure (Robson et al., 2022), previous studies based on semi-diurnal
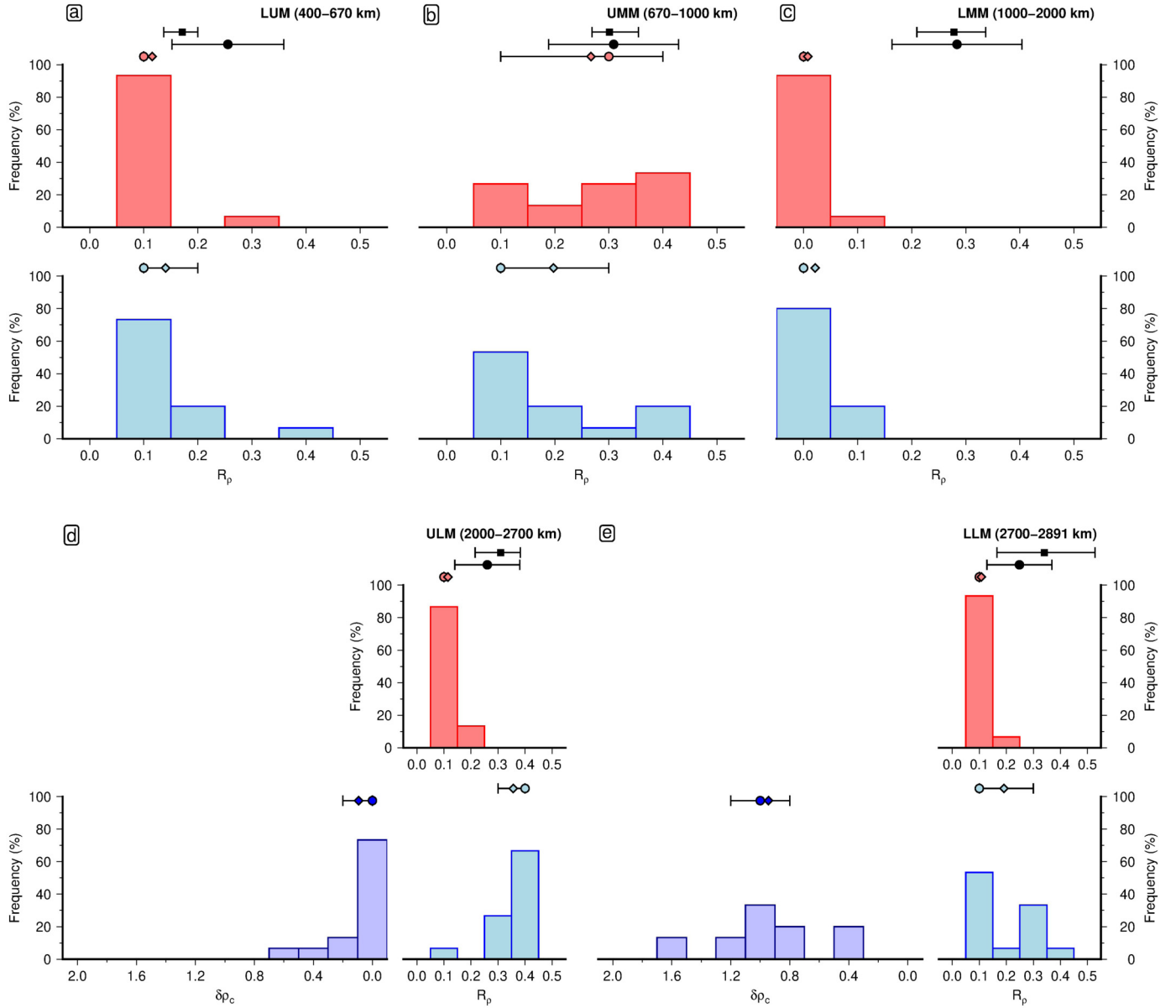
Fig. 4. Best-fitting R_ρ values for thermal and thermochemical models. (a) Lower upper mantle layer (400–670 km). Red bars = best-fitting R_ρ for thermal models; blue bars = best-fitting R_ρ for thermochemical models; coloured circles and error bars = medians and interquartile ranges; diamonds = mean weighted by total misfit, χ_G; black circle and error bars = predicted values and $\pm 2\sigma$ errors for a pyrolitic mantle composition, excluding post-perovskite (taken from Lu et al., 2020); black square and error bars = predicted values and $\pm 2\sigma$ errors for mantle compositions ranging from a mechanical mixture of 50% MORB and 50% pyrolite to 100% pyrolite, determined using Perple_X (Connolly, 2005; Stixrude and Lithgow-Bertelloni, 2011). In both cases, thermodynamic R_ρ predictions are corrected for anelasticity following methodology outlined in Lu et al. (2020) and Section S2.2. Note that frequencies refer to optimised thermal and thermochemical models (15 of each) in Tables S2 and S3. (b) Same for upper mid-mantle layer (670–1000 km). (c) Same for lower mid-mantle layer (1000–2000 km). (d) Same for upper lower mantle layer (2000–2700 km). Dark blue bars = best-fitting compositional density contrast, $\delta\rho_c$, for thermochemical models. (e) Same for lower lower mantle layer (2700–2891 km).

body tide and Stoneley mode splitting observations arrive at contrasting conclusions about LLVP density structure. The former show a clear preference for the presence of anomalously dense material, with trade-offs between the amplitude and depth distribution of excess density (Lau et al., 2017). In contrast, by also taking topography of the CMB into account, the latter prefer models with integrated density anomalies in the lower 400 km that are negative, as expected for a dominantly thermal control (Koelemeijer et al., 2017). In light of these studies, we next test whether the mantle structure obtained from our optimal TX2011-based geodynamic model with thermochemical variations, or its purely thermal counterpart, is most consistent with these geodetic and seismological observations.

3.1. Data and methods

3.1.1. Predicting semi-diurnal body tide responses

Simulating Earth's body tidal response requires models of 3D elastic, 3D density, and 1D anelastic structure (Lau et al., 2017). In the upper 400 km of the mantle, 3D elastic structure is determined using the calibrated parameterisation of SLNAAFSA to remove anelastic reductions in V_S from the seismic tomographic model, leaving only anharmonic V_S variations (V_S^{anh}). Below 300 km, V_S^{anh} is derived from the tomographic values, V_S^{anel}, using radial changes in shear attenuation, Q_S^{-1}, from PREM and the expression

$$V_S^{anel} = V_S^{anh} \left[1 - \frac{Q_S^{-1}}{2\tan(\pi\alpha/2)} \right] \tag{8}$$
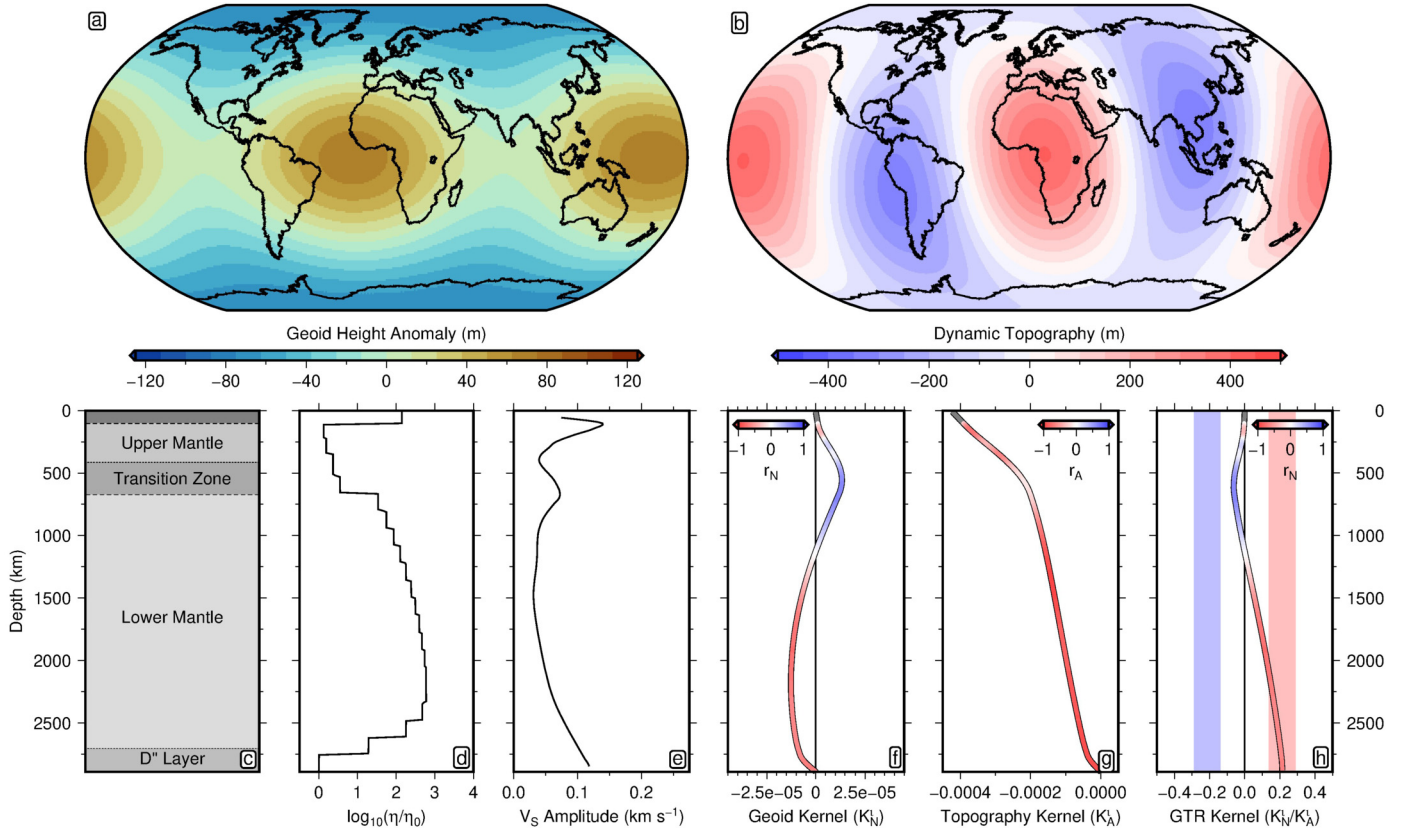
Fig. 5. Relationship between degree-two dynamic topography, geoid and V_S anomalies. (a) Observed non-hydrostatic geoid height anomalies (Chambat et al., 2010). (b) Observed water-loaded dynamic topography (Valentine and Davies, 2020). (c) Schematic radial mantle structure. (d) Normalised radial viscosity, η, profile (S10; Steinberger et al., 2010). (e) Spectral amplitude of $l = 2$ V_S anomalies from SEMUCB-WM1 tomographic model (French and Romanowicz, 2015). (f) Geoid kernel, K_N^l, coloured by geoid-to-V_S anomaly correlation, r_N, as a function of depth. (g) Dynamic topography kernel, K_A^l, coloured by dynamic topography-to-V_S anomaly correlation, r_A. (h) Geoid-to-topography ratio (GTR) kernel, coloured by r_N. Blue/red bands = values required to produce the observed GTR when thermal density anomalies are correlated/anti-correlated with the geoid.

where $\alpha = 0.15$ (Widmer et al., 1991). The resulting 3D V_S^{anh} model constrains the unrelaxed shear modulus. Unrelaxed bulk modulus variations are subsequently obtained from the anharmonic bulk sound velocity, V_ϕ^{anh}, assuming that

$$R_b = \frac{\partial \ln V_\phi}{\partial \ln V_S} \approx \frac{\partial \ln V_\phi^{anh}}{\partial \ln V_S^{anh}} = 0.05 \tag{9}$$

and that the radial V_ϕ^{anh} profile can be determined using the same V_S–V_ϕ scaling as PREM (Dziewonski and Anderson, 1981; Masters et al., 2000). The 1D anelastic structure applied to determine elastic modulus dispersion at the 12-hour period of the M2 body tide adopts the mean value of Q_S^{-1} obtained from the calibrated parameterisation of SLNAAFSA at depths above 400 km, and that of PREM at greater depths.

With the Earth model specified, the body tide response is computed using full-coupling normal mode perturbation theory, with shear and bulk moduli dispersion calculated at tidal frequencies using IERS standards (Petit and Luzum, 2013).

3.1.2. Predicting Stoneley mode splitting functions

To predict Stoneley mode splitting functions, 3D variations in V_S, V_P and CMB topography must be specified in addition to the density model. We follow the methodology of Koelemeijer et al. (2017) to derive V_P by scaling V_S anomalies from the input tomographic model using a constant value of $R_P = \partial \ln V_P / \partial \ln V_S = 0.5$ (Ritsema et al., 2004). We use mantle densities derived from the optimised V_S-to-density scalings obtained in Section 2.2, while CMB topography is taken from the associated instantaneous flow

prediction. These last two methodological features represent modifications to the Koelemeijer et al. (2017) study and constitute an improvement since the R_ρ values are more consistent with candidate chemical compositions for the deep mantle (as compiled by Lu et al., 2020) and the CMB deflections are now dynamically consistent with their respective LLVP density structure.

For a specified input velocity, density and topography model, Stoneley mode splitting coefficients, c^{st} are calculated using the expression

$$c_{st} = \int_0^{R_\oplus} d\ln\mathbf{m}_{st}(r) \cdot \mathbf{M}_s(r) r^2 dr + d\ln h_{st} H_s \tag{10}$$

where $d\ln\mathbf{m}_{st}(r)$ represents the prescribed 3D V_S, V_P, and density heterogeneity at spherical harmonic degree, s, order, t, and radius, r. Note that we use s and t rather than l and m for normal modes to avoid any confusion with the angular order l and azimuthal order m that define the normal mode of interest. $\mathbf{M}_s(r)$ are the relevant sensitivity kernels calculated using PREM (Woodhouse, 1980; Dziewonski and Anderson, 1981), $d\ln h_{st}$ describe the CMB topography variations (the discontinuity most important for Stoneley modes), and H_s is the associated sensitivity kernel at angular degree s. We note that, although Stoneley modes are sensitive to outer core structure, lateral variations in density and V_P are expected to be minimal within this layer (Stevenson, 1987), while any radial deviations from PREM would only affect the centre frequencies of the modes and not their splitting functions. Con-

sequently, we are confident that our conclusions are unaffected by plausible variations in outer core properties.

3.2. Results: fit to tidal and Stoneley mode data

Goodness-of-fit to semi-diurnal body tide constraints is calculated following the methodology of Lau et al. (2017), in which agreement between predicted and observed in-phase M2 body tide displacement is assessed at the sites of GPS stations by determining whether inclusion of 3D elastic and density structure significantly enhances the coherence between the two fields compared with a baseline 1D model (PREM; Dziewonski and Anderson, 1981). The 3D Earth model is only considered to yield a statistically significant improvement if the correlation obtained between 'raw' and 'corrected' GPS residuals exceeds that obtained for the 1D model at the 95% significance level, accounting for correlation between GPS estimates due to the uneven spatial distribution of receivers. Raw residuals represent observed M2 body tide displacements minus those predicted for the 1D model. Corrected residuals also account for the effects of Moho and CMB excess ellipticity, Earth rotation and ocean tidal loading, and, in the 3D model case, incorporate an additional correction for differences in the body tide displacement predicted using 3D versus 1D structure.

In a similar manner to the geodynamic observables, misfit between predicted and observed Stoneley mode splitting functions (Koelemeijer et al., 2013), χ_S, is assessed using

$$\chi_S = \frac{1}{N_S} \sum_{n_S=1}^{N_S} \frac{\sum_{s=2}^{s_{max}} \sum_{t=-s}^{s} \left(c_{st}^c - c_{st}^o\right)^2}{\sum_{s=2}^{s_{max}} \sum_{t=-s}^{s} \left(c_{st}^o\right)^2} \tag{11}$$

where $N_S = 9$ is the number of individual Stoneley modes investigated and the summation term over s includes only even degree terms, where s_{max} is the maximum order considered. Note that we use $s_{max} = 2$ in the calculations discussed here. The impact of setting s_{max} to the maximum degree at which splitting function measurements are available for each mode is tested in the Supplementary Information, as well as the consequences of adopting different misfit criteria (Section S1.4; Table S4) and ignoring the effect of CMB topography (Section S2.3; Fig. S13).

The improvement in fit to body tide observations obtained for the optimum TX2011-derived thermal model relative to the 1D reference case is only significant at the 93.8% level. By contrast, the best-fitting thermochemical density model based on the same tomographic input, but with chemical heterogeneity in the base of LLVPs, yields statistically significant outcomes at the 95.8% level. Similarly, we find that the misfit between observed and predicted Stoneley mode splitting functions is ~20% lower for the optimal TX2011-based thermochemical density model compared to its equivalent thermal model (Fig. S10; Table S4). This conclusion appears to contradict the findings of Koelemeijer et al. (2017), but is readily explained by our methodological improvements, as well as the stronger V_S amplitudes at $l = 2$ below 2500 km depth in TX2011 compared to the SP12RTS model adopted in that study (explored further in Section S1.4). Significantly, these results indicate that the presence of anomalously dense material in the bottom ~200 km of the LLVPs is not only compatible with available geodynamic constraints, but is also consistent with observations of Earth's semi-diurnal body tide and Stoneley mode splitting.

4. Compositional inversions

Having established that geodynamic, seismological, and geodetic constraints provide evidence for the presence of a dense basal layer within the LLVPs, we explore the compatibility of different candidate compositions. Several hypotheses have been proposed for the formation of chemically distinct LLVP material, including:

Table 1
Molar oxide ratios for different mantle compositional endmembers. All values are molar percentages. MORB = present-day mid-ocean ridge basalt; CEB = chondrite-enriched basalt; FSP = iron-enriched pyrolite; [1] = Workman and Hart (2005); [2] = Tolstikhin and Hofmann (2005); [3] = Lee et al. (2010).

Major Oxide	Pyrolite[1]	MORB[1]	CEB[2]	FSP[3]
SiO$_2$	38.71	51.75	48.47	40.15
MgO	49.85	14.94	20.00	41.98
FeO	6.17	7.06	11.28	12.90
CaO	2.94	13.88	10.59	2.82
Al$_2$O$_3$	2.22	8.16	11.28	1.92
Na$_2$O	0.11	2.18	1.50	0.23

slow accumulation of basalt from subducted slabs reaching the CMB (Niu, 2018); preservation of primordial mantle material segregated during top-down crystallisation of a basal magma ocean (Labrosse et al., 2007); subduction of iron- and silicon-rich Hadean crust along with a terrestrial regolith comprising chondritic and solar–wind-implanted material (Tolstikhin and Hofmann, 2005); pooling of dense, iron-rich melts generated in the primordial mantle transition zone (Lee et al., 2010); and even accumulation of iron oxide expelled from the Earth's core as it cools (Mittal et al., 2020). We have elected to exclude this last explanation since recent studies indicate that the total mass of iron-rich material exsolved from the cooling core throughout Earth history is likely less than ~ 1% of the mantle; sufficient to account for thin (tens of km) and patchy ultra-low velocity zones, but not LLVP basal layers (hundreds of km thick; Mittal et al., 2020). We also rule out bridgmanite- and silica-enriched material expelled from the core as a candidate composition (e.g., Helffrich et al., 2020) because our thermodynamic modelling suggests this component would be lighter than ambient pyrolite and have faster intrinsic V_S, properties that are incompatible with dense layer material. To test the compositional range encompassed by the other suggested scenarios, we have assembled three endmembers: i) present-day mid-ocean ridge basalt (MORB; lowest iron, highest silicon content; Workman and Hart, 2005); ii) chondrite-enriched Hadean basalt (intermediate iron and silicon; Tolstikhin and Hofmann, 2005); and iii) iron-enriched pyrolite (highest iron, lowest silicon), representing early Archaean melts generated in the transition zone or chemically modified late-stage basal magma ocean cumulates (Lee et al., 2010; Labrosse et al., 2007; Table 1).

4.1. Data and methods

For each compositional endmember, we perform thermodynamic modelling using the Perple_X Gibbs free energy minimisation software and the phase equilibrium database of Stixrude and Lithgow-Bertelloni (2011). We find that all options yield a positive density and negative shear-wave velocity anomaly with respect to ambient pyrolitic mantle at deep mantle temperatures and pressures (~ 2000–4000 K; ~ 110–140 GPa; Fig. S11). The amplitude of these anomalies varies, with modern basaltic material generating the weakest anomalies, while the most iron-rich primordial components produce the strongest anomalies. The relatively modest excess density below 2700 km recovered in our initial geodynamic inversions ($\overline{\delta\rho_c} = 0.4$–1.6%) is consistent with mechanical mixtures of pyrolite with either 30–80% modern MORB or 10–50% of either of the two iron-rich, primordial components. This excess density, however, falls below the ~2–4% threshold that is inferred to be necessary for long-term preservation of intra-LLVP chemical heterogeneity (Tackley, 2012; Jones et al., 2020). We therefore explore how a trade-off between the thickness of the basal layer and its excess density affects the fit to the geodynamic and seismic constraints, and which of the proposed chemical compositions are most compatible.

A suite of density models is determined from tomographic V_S variations for each candidate composition (Table 1). Unlike the initial class of models generated in Section 2.2 for geodynamic inversions (which use linear scaling factors to convert V_S anomalies into density), these models are generated using this thermodynamically self-consistent framework. For a given composition, we use Perple_X and the Stixrude and Lithgow-Bertelloni (2011) data compilation to generate a lookup table of anharmonic shear-wave velocities and densities by varying temperature as [300, 350, ..4500] K and pressure as [0., 0.1, ...140] GPa (Section S2.1). At each depth, temperature-dependent discontinuities in density and seismic velocity caused by phase transitions are smoothed by adopting the median temperature derivative across a $\pm 500\,^{\circ}$C swath either side of the geotherm. This procedure accounts for the limited seismic resolution of tomographic models, which inevitably blur abrupt changes in physical properties associated with phase transitions. Smoothed anharmonic velocities are then corrected for anelasticity with a Q profile determined using the approach outlined in Lu et al. (2020) (Section S2.2; Fig. S12). Having smoothed and corrected the V_S lookup table, velocities from a given seismic tomographic model can be converted into temperature at each depth, with values adjusted by a constant offset to ensure mean temperatures are consistent with the mantle geotherm. These temperatures are then used to extract the corresponding buoyancy structure from the smoothed density lookup table. In cases where compositions are not equivalent to a particular endmember, properties appropriate for a mechanical mixture of the two components are calculated using the Voigt-Reuss-Hill approximation to average the elastic moduli. When the composition of the LLVP is distinct from ambient mantle, temperatures and densities are determined separately for the two components and then combined into a single array, with the boundary corresponding to the -0.65% V_S anomaly contour (Torsvik et al., 2006; Lau et al., 2017). All models assume that the range of possible mantle compositions is some combination of pyrolite and a specific dense component; either mid-ocean ridge basalt (MORB; Workman and Hart, 2005), chondrite-enriched basalt (CEB; Tolstikhin and Hofmann, 2005), or iron-enriched pyrolite (FSP; Labrosse et al., 2007; Lee et al., 2010). For each component, we generate models for compositional enrichments of [0, 10, ..., 100]% and test basal layer thicknesses in 100 km increments from 100–900 km, as well as testing 50 km.

In the upper 300 km of the mantle, density structure is identical to the first class of models we generated in our geodynamic inversions (see Section 2). Below 400 km, densities are taken directly from the thermodynamically self-consistent parameterisation described above, whilst between 300 km and 400 km depth, densities derived from the two parameterisations are smoothly merged by taking their weighted average, as described for the first class of models. Since optimal thermal and thermochemical density models recovered from geodynamic inversions consistently find that R_ρ(LMM) ~ 0, density anomalies in the 1000–2000 km depth interval are set to zero for all models. We also test the effect of using a high-pass filter to remove degree-two structure to include only small-scale density anomalies within this depth range (Section S1.3; Fig. S15).

4.2. Results: models consistent with all observables

Instantaneous flow calculations are repeated with our suite of thermodynamically self-consistent density models for different combinations of chemical components within and outside the LLVPs. We find a strong trade-off between the anomalous density of the basal LLVP region and its thickness, with similar misfit values to geodynamic observables (χ_G) obtained for thin, highly enriched versus thicker, less chemically distinct basal layers

(Fig. S14a–c). Although results are dependent on the radial mantle viscosity profile, optimal fits are generally obtained for thinner, more enriched layers, irrespective of whether anomalously dense material within the LLVPs is assumed to be basaltic or primordial. Best-fitting models for each chemical component yield similar misfit values, with optimal layer thicknesses of $\sim$200 km. This finding is consistent with that of our initial geodynamic inversions, suggesting that the relatively simple, linear V_S-to-density scaling employed in those models yields a suitable first-order approximation of LLVP structure.

We also investigate the impact of combining the geodynamic misfit from Equation (7) with Stoneley mode misfit from Equation (11) into a joint misfit function, χ_T, using

$$\chi_T = w_G \chi_G + w_S \chi_S \tag{12}$$

where $w_G = 0.5$ and $w_S = 5$ are weightings that have been selected to yield comparable values at their respective global minima. This joint misfit function exhibits a similar trade-off between basal layer thickness and density (Figs. S13, S14, and S16). Nevertheless, while each endmember composition can generate density models that satisfy the 2–4% excess density threshold for long-term chemical heterogeneity preservation (Tackley, 2012; Jones et al., 2020), the two primordial candidates yield a $\sim 10\%$ reduction in joint misfit to Stoneley mode and geodynamic observations compared with recycled MORB (Fig. 6). Irrespective of whether the TX2011 or S40RTS tomographic model is used to generate density structure, optimal chondrite-enriched basaltic configurations give $\sim$5–10% lower misfit than their iron-enriched pyrolitic counterpart, indicating that a 100–200 km-thick layer, mainly composed of sequestered Hadean crust, is most consistent with currently available data (Supplementary Section S2.3; Figs. 6, S14, and S16).

5. Discussion

Although the uncertainty inherent to thermodynamic estimates of V_S and density means that our conclusion regarding basal layer composition is not definitive (Connolly and Khan, 2016), the presence of Hadean crust in these regions is consistent with several independent constraints. Firstly, time-dependent thermochemical convection studies suggest that, following subduction, ~ 10 km-thick present-day oceanic crust is easily re-entrained whereas an early-formed proto-crust with greater thickness and higher iron content could be more readily preserved within the base of LLVPs (Li and McNamara, 2013). Secondly, the elevated SiO_2 content of the primordial basaltic composition compared with the iron-enriched pyrolite helps to explain the observed spatial decorrelation between V_ϕ and V_S in the lowermost mantle, provided that bridgmanite is at least partially replaced by post-perovskite within this depth range (Fig. S11; Koelemeijer et al., 2018). Thirdly, the less extreme reduction in V_S at lowermost mantle conditions for primordial basalt ($\sim 2\%$), compared to iron-enriched pyrolite ($\sim 3\%$), is more compatible with the relatively modest V_S gradients that have been inferred across LLVP boundaries (Davies et al., 2012; Deschamps et al., 2012). Finally, when comparing observed and predicted V_S, V_P and V_ϕ signatures for a wide range of candidate LLVP compositions, Vilella et al. (2021) found that seismic constraints necessitate minimal quantities of ferropericlase (<6 vol%) and potentially large proportions of calcium-perovskite (up to ~ 35 vol%), consistent with expected phase assemblages for basaltic material at deep mantle conditions. Optimal compositions found by this latter study also feature elevated Al_2O_3 contents (3–13 wt%) and oxidation states ($Fe^{3+}/\sum Fe > 0.3$), which can be attributed to the addition of chondritic material and chemical partitioning during a shallow melting event (Zega et al., 2003; Herzberg, 2016; Zhang et al., 2017; Table 1).
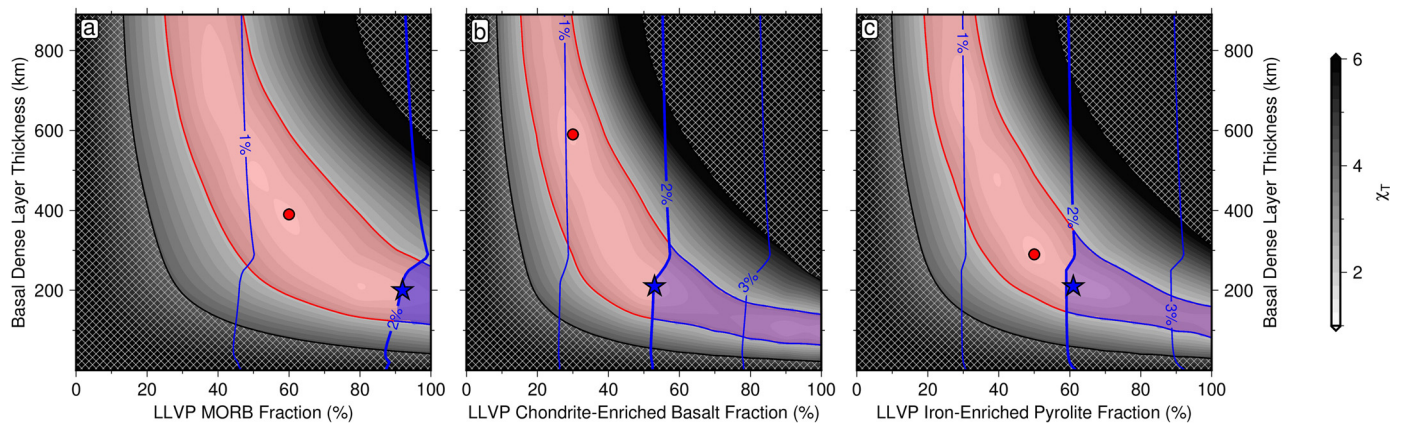
Fig. 6. Combined misfit to geodynamic and Stoneley mode observations as a function of mantle composition. (a) Combined total misfit (χ_T) as a function of MORB fraction within the LLVPs (Workman and Hart, 2005). Material outside the LLVPs is assumed to be pyrolitic. Hatched region = models with peak-to-valley $l = 2$ CMB topography exceeding ±4.7 km maximum constraint (Koelemeijer, 2021); red circle = best-fitting model ($\chi_T = 1.19$); red shading = models with misfit less than double that of global minimum; thin blue contours = intrinsic compositional density difference between dense layer material and ambient mantle; bold blue contour = lower limit of suggested ~2–4% compositional density threshold for long-term preservation of intra-LLVP chemical heterogeneity (Tackley, 2012; Jones et al., 2020); blue star = best-fitting model with intrinsic density anomaly above preservation threshold ($\chi_T = 1.49$); blue shading = models with misfit less than double that of global minimum and compositional density anomaly above preservation threshold. (b) Same for primordial material (chondrite-enriched basalt; Tolstikhin and Hofmann, 2005). Red circle = best-fitting model ($\chi_T = 1.21$); blue star = best-fitting model with intrinsic density anomaly above preservation threshold ($\chi_T = 1.31$). (c) Same for primordial material (iron-enriched pyrolite; Lee et al., 2010). Red circle = best-fitting model ($\chi_T = 1.14$); blue star = best-fitting model with intrinsic density anomaly above preservation threshold ($\chi_T = 1.37$). Calculations use seismic velocities from TX2011 to determine elastic and density structure and the S10 viscosity profile to compute the mantle flow field.

For the reasons listed above, we conclude that the most likely candidate for the chemically distinct, 100–200 km-thick basal layer is Hadean basaltic material (Tolstikhin and Hofmann, 2005). Nevertheless, more iron-rich and silicon-poor primordial endmembers, or mixtures of these components, cannot currently be discounted given the uncertainties associated with lower mantle seismic tomographic imaging, viscosity structure, and the inference of physical properties from seismic observations. We also note that the geodynamic, seismological, and geodetic constraints we use here are only sensitive to long-wavelength density variations. As a result, the dense material may be unevenly distributed within the basal layers and potentially concentrated beneath thermochemical plume clusters (e.g., Davaille and Romanowicz, 2020; Lu et al., 2020).

Sites of past and present intraplate volcanism with anomalous isotope ratios, including high ^{3}He/^{4}He ratios and positive μ^{182}W, have been shown to spatially correlate with LLVPs and have led to speculation that they may represent distinct chemical reservoirs within the deep mantle (White, 2015). Since all ^{3}He is of primordial origin and the decay of ^{182}Hf to ^{182}W has a half-life of only ~9 Myr, these chemical fingerprints indicate that this reservoir formed early in Earth history and has been largely isolated (i.e., relatively undegassed). Our finding that the basal ~100–200 km portions of the LLVPs most likely contain iron- and silicon-enriched primordial material, rather than accumulations of more youthful MORB, are therefore compatible with this view. This inference is further supported by the agreement between the approximate mass of these layers (3–6 × 10^{22} kg) and that of the primordial Earth reservoir inferred from ^{3}He/^{4}He ratios (~6.2 × 10^{22} kg; Tolstikhin and Hofmann, 2005). Finally, our finding that LLVP basal layers likely contain chondrite-enriched basalt, coupled with their relative thinness, is also consistent with geodynamic studies investigating the origin of systematic $\mu^{182}W$ differences between ocean island basalts and flood basalts erupted in large igneous provinces (Jones et al., 2019). Clearly further integration of geochemical and geophysical constraints is needed to confirm whether these thin basal layers represent Hadean crust, remnants of magmatic processes within the early Earth's interior, or a combination of both. Our proposed model of lower mantle density structure does, however, already provide a self-consistent explanation of a full range of geodynamic, geodetic, seismological, and geochemical constraints.

6. Conclusions

Determining the thermochemical properties and vertical extent of LLVP-related buoyancy anomalies is of fundamental importance to solving a range of outstanding controversies in Earth sciences, including the formation of mantle plumes, the origin of anomalous geochemical signatures in the basalts they produce, and the rate at which convectively supported topography grows and decays. By taking a multi-pronged approach that integrates a full range of geodynamic, geodetic and seismological data with numerical models, we are able to place valuable new constraints on LLVP structure. Firstly, by using recent measurements of Earth's dynamic topography, CMB ellipticity, and geoid to determine optimal models of mantle flow, we find that anomalously dense material is concentrated within the basal ~200 km of LLVPs, irrespective of the assumed tomographic and rheologic configuration. Secondly, we conclude that buoyancy variations associated with these seismically imaged features extend no more than ~900 km above the CMB. Thirdly, we show that the apparent disagreement between LLVP buoyancy structures previously inferred from Stoneley mode and body tide inversions can be resolved using our geodynamically optimised thermochemical models. Finally, by comparing an ensemble of thermodynamically self-consistent density models that cover a range of possible recycled and primordial compositions to a full suite of geodynamic, seismological, and geochemical constraints, we demonstrate that the dense basal material within the LLVPs likely comprises remnants of Hadean crust and chondritic regolith. These results confirm that basal sections of LLVPs are potential reservoirs for the primordial isotope signatures observed in oceanic island basalts.

Both the presence of dense primordial material within LLVPs and the limited vertical extent of their associated buoyancy (≤ 900 km above the CMB) have important implications for existing predictions of mantle evolution, reducing the amplitude and slowing the rate of change of surface dynamic topography. By adopting this structure and validating its associated mantle flow field against evidence for continent-scale uplift and subsidence encoded in the geological record, our understanding of Earth's internal dynamics can be greatly refined, allowing impacts on landscape evolution and palaeoclimatic shifts to be determined with unprecedented fidelity.

Authorship contribution statement

F.D.R. and M.J.H. conceived this study. F.D.R. designed, set up and processed geodynamical simulations and relevant input models in consultation with M.J.H. S.G. wrote software for computing instantaneous mantle flow. S.G. and M.J.H. developed tools for constructing anelastically corrected input density models from thermodynamic lookup tables. P.K. developed the computing infrastructure used to calculate predicted Stoneley mode splitting functions. H.C.P.L. developed the software to compute body tide responses and conducted statistical analysis of the outputs. F.D.R. and M.J.H. integrated interdisciplinary components. F.D.R. compiled the supplementary information and wrote the manuscript with M.J.H., following discussions with and contributions from all authors.

CRediT authorship contribution statement

Fred D. Richards: Conceptualization, Formal analysis, Investigation, Methodology, Software, Visualization, Writing – original draft, Writing – review & editing. **Mark J. Hoggard:** Conceptualization, Formal analysis, Methodology, Software, Writing – original draft, Writing – review & editing. **Sia Ghelichkhan:** Formal analysis, Software, Writing – review & editing. **Paula Koelemeijer:** Formal analysis, Software, Writing – review & editing. **Harriet C.P. Lau:** Formal analysis, Software, Writing – review & editing.

Declaration of competing interest

The authors declare that they have no known competing financial interests or personal relationships that could have appeared to influence the work reported in this paper.

Data availability

Datasets used in this study are publicly available from cited references. The mantle density models and mantle flow predictions generated in this study are available from the authors on request.

Acknowledgements

Appendix A. Supplementary material

Supplementary material related to this article can be found online at https://doi.org/10.1016/j.epsl.2022.117964.

References

Arevalo Jr., R., McDonough, W.F., Stracke, A., Willbold, M., Ireland, T.J., Walker, R.J., 2013. Simplified mantle architecture and distribution of radiogenic power. Geochem. Geophys. Geosyst. 14 (7), 2265–2285.

Auer, L., Boschi, L., Becker, T., Nissen-Meyer, T., Giardini, D., 2014. Savani: a variable resolution whole-mantle model of anisotropic shear velocity variations based on multiple data sets. J. Geophys. Res., Solid Earth 119 (4), 3006–3034.

Burke, K., Steinberger, B., Torsvik, T.H., Smethurst, M.A., 2008. Plume generation zones at the margins of large low shear velocity provinces on the core–mantle boundary. Earth Planet. Sci. Lett. 265 (1–2), 49–60.

Chambat, F., Ricard, Y., Valette, B., 2010. Flattening of the Earth: further from hydrostaticity than previously estimated. Geophys. J. Int. 183 (2), 727–732.

Connolly, J.A.D., 2005. Computation of phase equilibria by linear programming: a tool for geodynamic modeling and its application to subduction zone decarbonation. Earth Planet. Sci. Lett. 236 (1–2), 524–541.

Connolly, J.A.D., Khan, A., 2016. Uncertainty of mantle geophysical properties computed from phase equilibrium models. Geophys. Res. Lett. 43 (10), 5026–5034.

Corrieu, V., Thoraval, C., Ricard, Y., 1995. Mantle dynamics and geoid Green functions. Geophys. J. Int. 120 (2), 516–523.

Cottaar, S., Lekic, V., 2016. Morphology of seismically slow lower-mantle structures. Geophys. J. Int. 207 (2), 1122–1136.

Davaille, A., Romanowicz, B., 2020. Deflating the LLSVPs: bundles of mantle thermochemical plumes rather than thick stagnant "Piles". Tectonics 39 (10), e2020TC006265.

Davies, D.R., Goes, S., Davies, J.H., Schuberth, B., Bunge, H.-P., Ritsema, J., 2012. Reconciling dynamic and seismic models of Earth's lower mantle: the dominant role of thermal heterogeneity. Earth Planet. Sci. Lett. 353, 253–269.

Dehant, V., Laguerre, R., Rekier, J., Rivoldini, A., Triana, S.A., Trinh, A., Van Hoolst, T., Zhu, P., 2017. Understanding the effects of the core on the nutation of the Earth. Geod. Geodyn. 8 (6), 389–395.

Deschamps, F., Cobden, L., Tackley, P.J., 2012. The primitive nature of large low shear-wave velocity provinces. Earth Planet. Sci. Lett. 349, 198–208.

Dziewonski, A.M., Anderson, D.L., 1981. Preliminary reference Earth model. Phys. Earth Planet. Inter. 25 (4), 297–356.

Forte, A.M., Quéré, S., Moucha, R., Simmons, N.A., Grand, S.P., Mitrovica, J.X., Rowley, D.B., 2010. Joint seismic–geodynamic–mineral physical modelling of African geodynamics: a reconciliation of deep-mantle convection with surface geophysical constraints. Earth Planet. Sci. Lett. 295 (3–4), 329–341.

French, S.W., Romanowicz, B., 2015. Broad plumes rooted at the base of the Earth's mantle beneath major hotspots. Nature 525 (7567), 95–99.

Garnero, E.J., McNamara, A.K., Shim, S.-H., 2016. Continent-sized anomalous zones with low seismic velocity at the base of Earth's mantle. Nat. Geosci. 9 (7), 481–489.

Grand, S.P., 2002. Mantle shear–wave tomography and the fate of subducted slabs. Philos. Trans. R. Soc. Lond. A, Math. Phys. Eng. Sci. 360 (1800), 2475–2491.

Gurnis, M., Mitrovica, J.X., Ritsema, J., van Heijst, H.-J., 2000. Constraining mantle density structure using geological evidence of surface uplift rates: the case of the African superplume. Geochem. Geophys. Geosyst. 1 (7), 1999GC000035.

Gwinn, C.R., Herring, T.A., Shapiro, I.I., 1986. Geodesy by radio interferometry: studies of the forced nutations of the Earth: 2. Interpretation. J. Geophys. Res., Solid Earth 91 (B5), 4755–4765.

Hager, B.H., Clayton, R.W., Richards, M.A., Comer, R.P., Dziewonski, A.M., 1985. Lower mantle heterogeneity, dynamic topography and the geoid. Nature 313 (6003), 541–545.

Helffrich, G., Hirose, K., Nomura, R., 2020. Thermodynamical modeling of liquid Fe-Si-Mg-O: Molten magnesium silicate release from the core. Geophys. Res. Lett. 47 (21), e2020GL089.

Herzberg, C., 2016. Petrological evidence from komatiites for an early Earth carbon and water cycle. J. Petrol. 57 (11–12), 2271–2288.

Hoggard, M.J., Czarnota, K., Richards, F.D., Huston, D.L., Jaques, A.L., Ghelichkhan, S., 2020. Global distribution of sediment-hosted metals controlled by craton edge stability. Nat. Geosci. 13, 504–510.

Hoggard, M.J., White, N., Al-Attar, D., 2016. Global dynamic topography observations reveal limited influence of large-scale mantle flow. Nat. Geosci. 9, 456–463.

Hoggard, M.J., Winterbourne, J., Czarnota, K., White, N., 2017. Oceanic residual depth measurements, the plate cooling model, and global dynamic topography. J. Geophys. Res., Solid Earth 122 (3), 2328–2372.

Jones, T.D., Davies, D.R., Sossi, P., 2019. Tungsten isotopes in mantle plumes: heads it's positive, tails it's negative. Earth Planet. Sci. Lett. 506, 255–267.

Jones, T.D., Maguire, R.R., van Keken, P.E., Ritsema, J., Koelemeijer, P., 2020. Subducted oceanic crust as the origin of seismically slow lower-mantle structures. Prog. Earth Planet. Sci. 7, 1–16.

Jordan, T.H., 1978. Composition and development of the continental tectosphere. Nature 274 (5671), 544–548.

Koelemeijer, P., 2021. Towards consistent seismological models of the core-mantle boundary landscape. In: Marquardt, H., Ballmer, M., Cottaar, S., Konter, J.G. (Eds.), Mantle Convection and Surface Expressions. In: Geophysical Monograph Series, vol. 263. Wiley Online Library, pp. 229–255.

Koelemeijer, P., Deuss, A., Ritsema, J., 2013. Observations of core-mantle boundary Stoneley modes. Geophys. Res. Lett. 40 (11), 2557–2561.

Koelemeijer, P., Deuss, A., Ritsema, J., 2017. Density structure of Earth's lowermost mantle from Stoneley mode splitting observations. Nat. Commun. 8 (1), 1–10.

Koelemeijer, P., Schuberth, B., Davies, D., Deuss, A., Ritsema, J., 2018. Constraints on the presence of post-perovskite in Earth's lowermost mantle from tomographic-geodynamic model comparisons. Earth Planet. Sci. Lett. 494, 226–238.

Labrosse, S., Hernlund, J., Coltice, N., 2007. A crystallizing dense magma ocean at the base of the Earth's mantle. Nature 450 (7171), 866–869.

Lau, H.C., Mitrovica, J.X., Davis, J.L., Tromp, J., Yang, H.-Y., Al-Attar, D., 2017. Tidal tomography constrains Earth's deep-mantle buoyancy. Nature 551 (7680), 321–326.

Lee, C.-T.A., Luffi, P., Höink, T., Li, J., Dasgupta, R., Hernlund, J., 2010. Upside-down differentiation and generation of a 'primordial' lower mantle. Nature 463 (7283), 930–933.

Li, M., McNamara, A.K., 2013. The difficulty for subducted oceanic crust to accumulate at the Earth's core-mantle boundary. J. Geophys. Res., Solid Earth 118 (4), 1807–1816.

Liu, X., Zhong, S., 2016. Constraining mantle viscosity structure for a thermochemical mantle using the geoid observation. Geochem. Geophys. Geosyst. 17 (3), 895–913.

Lu, C., Forte, A.M., Simmons, N.A., Grand, S.P., Kajan, M.N., Lai, H., Garnero, E.J., 2020. The sensitivity of joint inversions of seismic and geodynamic data to mantle viscosity. Geochem. Geophys. Geosyst. 21 (4), e2019GC008648.

Masters, G., Laske, G., Bolton, H., Dziewonski, A., 2000. The relative behavior of shear velocity, bulk sound speed, and compressional velocity in the mantle: implications for chemical and thermal structure. In: Karato, S.-I., Forte, A., Liebermann, R., Masters, G., Stixrude, L. (Eds.), Earth's Deep Interior: Mineral Physics and Tomography from the Atomic to the Global Scale. In: Geophysical Monograph Series, vol. 117. Wiley Online Library, pp. 63–87.

Mittal, T., Knezek, N., Arveson, S.M., McGuire, C.P., Williams, C.D., Jones, T.D., Li, J., 2020. Precipitation of multiple light elements to power Earth's early dynamo. Earth Planet. Sci. Lett. 532, 116030.

Moucha, R., Forte, A., Mitrovica, J., Daradich, A., 2007. Lateral variations in mantle rheology: implications for convection related surface observables and inferred viscosity models. Geophys. J. Int. 169 (1), 113–135.

Moulik, P., Ekström, G., 2016. The relationships between large-scale variations in shear velocity, density, and compressional velocity in the Earth's mantle. J. Geophys. Res., Solid Earth 121 (4), 2737–2771.

Ni, S., Tan, E., Gurnis, M., Helmberger, D., 2002. Sharp sides to the African superplume. Science 296 (5574), 1850–1852.

Niu, Y., 2018. Origin of the LLSVPs at the base of the mantle is a consequence of plate tectonics – a petrological and geochemical perspective. Geosci. Front. 9 (5), 1265–1278.

Petit, G., Luzum, B., 2013. The 2010 reference edition of the IERS conventions. In: Reference Frames for Applications in Geosciences. Springer, pp. 57–61.

Richards, F.D., Hoggard, M.J., White, N., Ghelichkhan, S., 2020. Quantifying the relationship between short-wavelength dynamic topography and thermomechanical structure of the upper mantle using calibrated parameterization of anelasticity. J. Geophys. Res., Solid Earth 125 (9), e2019JB019062.

Ritsema, J., Deuss, A., Van Heijst, H.J., Woodhouse, J.H., 2011. S40RTS: a degree-40 shear-velocity model for the mantle from new Rayleigh wave dispersion, teleseismic traveltime and normal-mode splitting function measurements. Geophys. J. Int. 184, 1223–1236.

Ritsema, J., McNamara, A.K., Bull, A.L., 2007. Tomographic filtering of geodynamic models: implications for model interpretation and large-scale mantle structure. J. Geophys. Res., Solid Earth 112 (B1).

Ritsema, J., van Heijst, H.J., Woodhouse, J.H., 2004. Global transition zone tomography. J. Geophys. Res., Solid Earth 109 (B2), B02302.

Robson, A., Lau, H.C.P., Koelemeijer, P., Romanowicz, B., 2022. An analysis of core–mantle boundary Stoneley mode sensitivity and sources of uncertainty. Geophys. J. Int. 228 (3), 1962–1974.

Schaeffer, A.J., Lebedev, S., 2013. Global shear speed structure of the upper mantle and transition zone. Geophys. J. Int. 194 (1), 417–449.

Schuberth, B.S.A., Bunge, H.P., Steinle-Neumann, G., Moder, C., Oeser, J., 2009. Thermal versus elastic heterogeneity in high-resolution mantle circulation models with pyrolite composition: high plume excess temperatures in the lowermost mantle. Geochem. Geophys. Geosyst. 10 (1), Q01W01.

Simmons, N., Myers, S., Johannesson, G., Matzel, E., Grand, S., 2015. Evidence for long-lived subduction of an ancient tectonic plate beneath the southern Indian Ocean. Geophys. Res. Lett. 42 (21), 9270–9278.

Simmons, N.A., Forte, A.M., Grand, S.P., 2009. Joint seismic, geodynamic and mineral physical constraints on three-dimensional mantle heterogeneity: implications for the relative importance of thermal versus compositional heterogeneity. Geophys. J. Int. 177 (3), 1284–1304.

Steinberger, B., Conrad, C.P., Tutu, A.O., Hoggard, M.J., 2019. On the amplitude of dynamic topography at spherical harmonic degree two. Tectonophysics 760, 221–228.

Steinberger, B., Holme, R., 2008. Mantle flow models with core-mantle boundary constraints and chemical heterogeneities in the lowermost mantle. J. Geophys. Res., Solid Earth 113 (B5), B05403.

Steinberger, B., Werner, S.C., Torsvik, T.H., 2010. Deep versus shallow origin of gravity anomalies, topography and volcanism on Earth, Venus and Mars. Icarus 207 (2), 564–577.

Stevenson, D., 1987. Limits on lateral density and velocity variations in the Earth's outer core. Geophys. J. Int. 88 (1), 311–319.

Stixrude, L., Lithgow-Bertelloni, C., 2011. Thermodynamics of mantle minerals–II. Phase equilibria. Geophys. J. Int. 184 (3), 1180–1213.

Tackley, P.J., 2012. Dynamics and evolution of the deep mantle resulting from thermal, chemical, phase and melting effects. Earth-Sci. Rev. 110 (1–4), 1–25.

Tolstikhin, I., Hofmann, A.W., 2005. Early crust on top of the Earth's core. Phys. Earth Planet. Inter. 148 (2–4), 109–130.

Torsvik, T.H., Smethurst, M.A., Burke, K., Steinberger, B., 2006. Large igneous provinces generated from the margins of the large low-velocity provinces in the deep mantle. Geophys. J. Int. 167 (3), 1447–1460.

Valentine, A.P., Davies, D.R., 2020. Global models from sparse data: a robust estimate of Earth's residual topography spectrum. Geochem. Geophys. Geosyst. 21 (8), e2020GC009240.

Vilella, K., Bodin, T., Boukaré, C.-E., Deschamps, F., Badro, J., Ballmer, M.D., Li, Y., 2021. Constraints on the composition and temperature of LLSVPs from seismic properties of lower mantle minerals. Earth Planet. Sci. Lett. 554, 116685.

Watkins, C.E., Conrad, C.P., 2018. Constraints on dynamic topography from asymmetric subsidence of the mid-ocean ridges. Earth Planet. Sci. Lett. 484, 264–275.

Watts, A., Moore, J., 2017. Flexural isostasy: constraints from gravity and topography power spectra. J. Geophys. Res., Solid Earth 122 (10), 8417–8430.

White, W.M., 2015. Isotopes, DUPAL, LLSVPs, and anekantavada. Chem. Geol. 419, 10–28.

Widmer, R., Masters, G., Gilbert, F., 1991. Spherically symmetric attenuation within the Earth from normal mode data. Geophys. J. Int. 104 (3), 541–553.

Woodhouse, J., 1980. The coupling and attenuation of nearly resonant multiplets in the Earth's free oscillation spectrum. Geophys. J. Int. 61 (2), 261–283.

Workman, R.K., Hart, S.R., 2005. Major and trace element composition of the depleted MORB mantle (DMM). Earth Planet. Sci. Lett. 231 (1–2), 53–72.

Yamauchi, H., Takei, Y., 2016. Polycrystal anelasticity at near-solidus temperatures. J. Geophys. Res., Solid Earth 121 (11), 7790–7820.

Zega, T.J., Garvie, L.A., Buseck, P.R., 2003. Nanometer-scale measurements of iron oxidation states of cronstedtite from primitive meteorites. Am. Mineral. 88 (7), 1169–1172.

Zhang, H., Hirschmann, M., Cottrell, E., Withers, A., 2017. Effect of pressure on $Fe^{3+}/\Sigma Fe$ ratio in a mafic magma and consequences for magma ocean redox gradients. Geochim. Cosmochim. Acta 204, 83–103.